



TITLE:

Formation of metallic cation-oxygen network for anomalous thermal expansion coefficients in binary phosphate glass

AUTHOR(S):

Onodera, Yohei; Kohara, Shinji; Masai, Hirokazu; Koreeda, Akitoshi; Okamura, Shun; Ohkubo, Takahiro

CITATION:

Onodera, Yohei ...[et al]. Formation of metallic cation-oxygen network for anomalous thermal expansion coefficients in binary phosphate glass. Nature Communications 2017, 8: 15449.

ISSUE DATE:

2017-05-31

URL:

<http://hdl.handle.net/2433/225118>

RIGHT:

© The Author(s) 2017. This work is licensed under a Creative Commons Attribution 4.0 International License. The images or other third party material in this article are included in the article's Creative Commons license, unless indicated otherwise in the credit line; if the material is not included under the Creative Commons license, users will need to obtain permission from the license holder to reproduce the material. To view a copy of this license, visit <http://creativecommons.org/licenses/by/4.0/>



ARTICLE

Received 28 Oct 2016 | Accepted 29 Mar 2017 | Published 31 May 2017

DOI: 10.1038/ncomms15449

OPEN

Formation of metallic cation-oxygen network for anomalous thermal expansion coefficients in binary phosphate glass

Yohei Onodera^{1,2}, Shinji Kohara^{2,3,4,5}, Hirokazu Masai^{6,†}, Akitoshi Koreeda⁷, Shun Okamura⁶
& Takahiro Ohkubo⁸

Understanding glass structure is still challenging due to the result of disorder, although novel materials design on the basis of atomistic structure has been strongly demanded. Here we report on the atomic structures of the zinc phosphate glass determined by reverse Monte Carlo modelling based on diffraction and spectroscopic data. The zinc-rich glass exhibits the network formed by ZnO_x (averaged $x < 4$) polyhedra. Although the elastic modulus, refractive index and glass transition temperature of the zinc phosphate glass monotonically increase with the amount of ZnO , we find for the first time that the thermal expansion coefficient is very sensitive to the substitution of the phosphate chain network by a network consisting of Zn-O units in zinc-rich glass. Our results imply that the control of the structure of intermediate groups may enable new functionalities in the design of oxide glass materials.

¹ Research Reactor Institute, Kyoto University 2-1010 Asashiro-nishi, Kumatori-cho, Sennan-gun 590-0494, Japan. ² Light/Quantum Beam Field, Research Center for Advanced Measurement and Characterization, National Institute for Materials Science (NIMS), 1-1-1 Kouto, Sayo-cho, Sayo-gun 679-5148, Japan. ³ Information Integrated Materials Design Field, Center for Materials Research by Information Integration, NIMS, 1-2-1 Sengen, Tsukuba 305-0047, Japan. ⁴ PRESTO, Japan Science and Technology Agency, 7 Gobancho, Chiyoda-ku, Tokyo 102-0076, Japan. ⁵ Research and Utilization Division, Japan Synchrotron Radiation Research Institute/SPring-8, 1-1-1 Kouto, Sayo-cho 679-5198, Japan. ⁶ Institute for Chemical Research, Kyoto University, Gokasho, Uji 611-0011, Japan. ⁷ Department of Physical Sciences, Ritsumeikan University, 1-1-1 Nojihigashi, Kusatsu 525-8577, Japan. ⁸ Graduate School & Faculty of Engineering, Chiba University, 1-33, Yayoi-cho, Chiba 263-8522, Japan. † Present address: Department of Materials and Chemistry, National Institute of Advanced Industrial Science and Technology (AIST), 1-8-31 Midorigaoka, Ikeda, Osaka 563-8577, Japan. Correspondence and requests for materials should be addressed to S.K. (email: KOHARA.Shinji@nims.go.jp) or to H.M. (email: hirokazu.masai@aist.go.jp).

Oxide glass prepared by melt-quenching is usually composed of network former (NWF) and network modifier (NWM) groups¹. SiO₂ is a typical NWF oxide that constitutes the ring structures, which are formed from SiO₄ tetrahedra². Alkali silicate glass consisting of an alkali oxide as NWM and SiO₂ as NWF is a representative oxide glass and it is widely used in industrial applications such as photonic and electronic devices. Furthermore, structural modification of the SiO₄ tetrahedral network in alkali silicate glasses has been extensively studied both experimentally and theoretically^{3–6} to clarify structure–property relations of glasses.

P₂O₅ is generally classified as NWF groups along with SiO₂, B₂O₃ and GeO₂ from the viewpoint of glass-forming ability. However, P₂O₅ differs from other NWF oxides since the P=O bond allows the delocalized electrons in phosphate glasses^{7–10}. On the other hand, several studies have shown that the main glass network^{11,12} of non-conventional phosphate glass, that is, so-called invert glass, is composed of a counter metal oxide. Previous studies have suggested that the local structure of the PO₄ unit does not always act as a NWF, and that its structure depends on the chemical composition of the glass. However, the detailed structure of the glass network has not been fully understood due to the lack of experimental information, which, in turn, is the result of disorder. Phosphate glass is often considered for practical applications because of its durability¹³, but has significant potential for application to several other uses, owing to its unique physical and structural properties^{14–18}. Understanding the network structure of a phosphate glass system is therefore one of the most important unresolved issues facing glass science.

In contrast to the conventional NWF group, several metal oxides, which are classified as intermediate groups, can act as either NWF or NWM groups¹, depending on the number of NWF units, that is, the glass composition. This suggests that the conventional glass-forming theory cannot explain the behaviour of the intermediate group of oxide glass. Zinc oxide is classified as being part of the intermediate group. In the case of zinc phosphate (ZP), monolithic bulk glass can be obtained although the P₂O₅ content is <33.3 mol% (that is, less than that of pyro-ZP). ZP exhibits low-melting-point properties and does not contain any hazardous cations, such as lead. Therefore, ZP glass is a promising material for use as lead-free sealing glass^{19,20}. Recently, ZP glass has also been shown to be a good host for emitting centres^{21–24} and is, therefore, a potential candidate for next-generation optical materials. In fact, these types of glass exhibit high transparency in the ultraviolet region; for example, the 60ZnO–40P₂O₅ glass has an optical absorption edge of over 6 eV, which stems from the O–Zn charge transfer transition²⁵. The bandgap of ZP glass is, however, much wider than expected especially when that (at 3.4 eV) of the wurtzite ZnO crystal with Zn–O four coordination is considered²⁶. The four-coordinated state of Zn is believed to result from its having a similar coordination to that of the ZnO crystal. The structure of ZP glass, particularly that of 60ZnO–40P₂O₅, has been extensively analysed using X-ray photoelectron spectroscopy^{27,28}, ³¹P nuclear magnetic resonance (NMR)^{29–31}, X-ray or neutron diffraction^{32–34}, high-performance liquid chromatography analysis³⁵, Raman and infrared spectroscopy³⁶, as well as molecular dynamics simulation³⁷. Several groups have also performed structural analyses using neutron and X-ray diffraction with the aid of reverse Monte Carlo (RMC) modelling^{34,38,39}. Those studies revealed the zinc in the ZP glass to be in the four-coordinated state.

However, previous investigations have shown that metal oxide has a small oxygen coordination in glass^{40–43}, since the rigid glass network enables the metastable species of metal oxide to be

sustained in the glass matrix. Therefore, the modelling of a reliable atomic arrangement in glass based on metal–cation-specific experimental data and conventional diffraction data is essential. As such, in this article, we report on the reliable atomic configuration of ZP glass from the viewpoint of three-dimensional (3D) network linkage, that is, the connectivity of each oxide. We use a combination of ³¹P magic angle spinning (MAS) NMR, Zn *K*-edge extended X-ray absorption fine structure (EXAFS), as well as X-ray and neutron diffraction data³⁸ to determine the dependence of this connectivity on the chemical composition and on the zinc coordination. Moreover, we discuss the relationship between several properties and glass structure and find that the thermal expansion coefficient is sensitive to the substitution of the phosphate chain network by a network consisting of Zn–O units in zinc-rich glass.

Results

Sample characterization and physicochemical properties. First of all, it is ensured that nanocrystallites are not precipitated in transparent *x*ZnO–(100–*x*)P₂O₅ (*x*ZP) glass prepared by the melt-quench method. The chemical compositions of ZP glasses were determined by using inductively coupled plasma-atomic emission spectrometry analysis (Supplementary Fig. 1 and Supplementary Table 1). It is confirmed that the compositions of our samples are precise. Supplementary Table 2 summarizes the glass transition temperature *T*_g, density, molar volume, refractive indices and the longitudinal sound velocity *V*_L of ZP glass. As the table indicates, the *T*_g, density and refractive index increase with the amount of ZnO. Supplementary Fig. 2 shows that the longitudinal modulus *c*₁₁ also increases with the amount of ZnO, while the molar volume decreases.

Figure 1a shows the thermal expansion curves for 58ZP, 60ZP, 65ZP and 70ZP glass. The bending points of the curves correspond to the *T*_g listed in Supplementary Table 2. Figure 1b shows linear thermal expansion coefficients of these glasses as a function of ZnO amount. The thermal expansion coefficients increase with increasing ZnO fraction. If the glass network is similar, that is, if the glass has the same NWF, the lower *T*_g glass generally exhibits a higher thermal expansion coefficient^{44,45}. However, the obtained results show that the higher *T*_g glass exhibits a higher thermal expansion coefficient. The anomaly of thermal expansion coefficients suggests that the glass networks might be changed, although the *T*_g and *c*₁₁ values changed linearly depending on the chemical composition (Supplementary Table 2).

NMR spectroscopy and EXAFS. NMR spectroscopic measurements were used to obtain the information on the local structure in glasses. The ³¹P MAS NMR spectra of *x*ZP glass (Fig. 2a) exhibit peaks that correspond to the Q⁰ (3 p.p.m.), Q¹ (–11 p.p.m.) and Q² (–30 p.p.m.) units, which are commonly observed in ZP glass^{29–31,46}. However, peaks corresponding to the Q³ unit are absent from the spectra. The ratio of Q^{*n*} units, as calculated from the area of each peak, shows (Fig. 2b) that the number of Q² chains decreases significantly as the amount of ZnO increases. The results of our NMR are in line with the results of high-performance liquid chromatography analysis³⁵, indicating that the PO₄ units no longer form a glass network, especially for 70ZP glass, as was recently suggested by Hoppe *et al.*³⁹.

We also determined the Zn–O coordination number and subsequently the local oxygen coordination of zinc. The EXAFS spectra, *k*³χ(*k*), of the different types of ZP glass are shown in Fig. 3a. As the figure shows, the oscillation and the period of the oscillation are slightly attenuated at high *k* values and shift

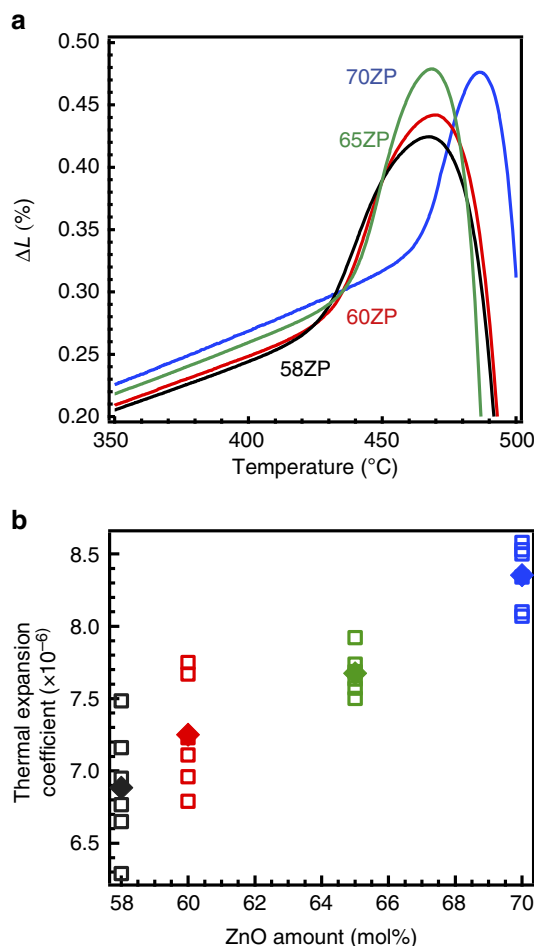


Figure 1 | Linear thermal expansion coefficients of the ZP glass.

(a) Thermal expansion curves of 58ZP, 60ZP, 65ZP and 70ZP glasses. (b) Thermal expansion coefficients below the T_g as a function of ZnO. The 70ZP glass exhibits higher T_g as well as higher thermal expansion coefficient below and above the T_g , compared to those of 60ZP glass. Closed squares indicate each mean value.

towards the low k region as the amount of ZnO increases. The Fourier-transformed (FT) EXAFS spectra of the x ZP glass, shown in Fig. 3b, exhibit one prominent peak, that is, the peak corresponding to the first coordination of the glass. Supplementary Table 3 summarizes the atomic distance and Debye–Waller factor, coordination number, N_{ZnO} , of the Zn–O in the glass. We estimated the values by fitting the first coordination shell in the EXAFS spectra and obtained an atomic distance and N_{ZnO} of ~ 1.96 – 1.97 Å and < 4 , respectively. This small oxygen coordination is different from those obtained from X-ray and neutron diffraction with the aid of RMC modelling^{34,38,39}.

Structure modelling. We performed RMC modelling using X-ray diffraction, neutron diffraction³⁸ and EXAFS data with several coordination number constraints to identify several chemical coordination states around phosphorus, based on the results of ^{31}P MAS NMR, to reveal the behaviour of the oxygen coordination around zinc. Figure 4 shows that there is good agreement between the RMC-modelled and experimentally determined X-ray and neutron structure factors, $S(Q)$ and EXAFS $k^3\chi(k)$, of the 60ZP and the 70ZP glasses. The partial structure factors, $S_{ij}(Q)$, calculated from the RMC models are shown in Supplementary Fig. 3. The 60ZP and the 70ZP glasses have almost identical $S_{\text{PO}}(Q)$, $S_{\text{OO}}(Q)$ and $S_{\text{ZnO}}(Q)$, indicating

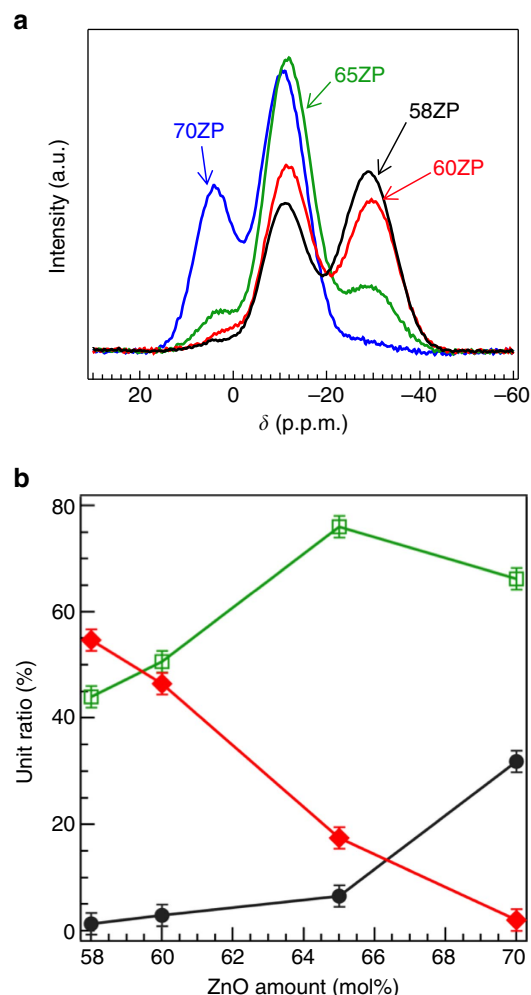


Figure 2 | ^{31}P MAS NMR spectra of the ZP glass. (a) ^{31}P MAS NMR spectra and (b) Q^n distribution. The peak areas are normalized using the amount of P_2O_5 . The error bars in b represent s.d. of each peak area obtained from deconvolution of ^{31}P MAS NMR spectra.

that the different types of ZP glass have the same short-range structure. This similarity can also be clearly observed in the partial-pair correlation functions, $g_{ij}(r)$, shown in Supplementary Fig. 4. On the other hand, the $S_{\text{PP}}(Q)$, $S_{\text{PZn}}(Q)$ and $S_{\text{ZnZn}}(Q)$ differ significantly, indicating the substantial difference between the connectivity of the short-range structural units, PO_4 tetrahedra and Zn–O polyhedra in the 60ZP and the 70ZP glasses. This behaviour is consistent with the NMR data, which reveal a significant reduction of Q^2 species in the 70ZP glass. In addition, N_{ZnO} of 3.6 and 3.8 were calculated at atomic distances of up to 2.4 Å for 60ZP and 70ZP glasses, respectively. The Zn–O coordination numbers obtained from RMC modelling agree with the data determined experimentally by EXAFS, which is very sensitive to the Zn–O coordination, but are smaller than some of the values reported in previous studies^{34,37,38}. To confirm the reduced Zn–O coordination in the glass, the FT EXAFS spectra and neutron total correlation functions $T(r)$ for the different types of ZP glass were compared with those of ZnO and β - $\text{Zn}_2\text{P}_2\text{O}_7$ crystals. As can be seen in Supplementary Fig. 5a, the Zn–O atomic distance in FT EXAFS spectra of the ZP glass is slightly shorter than that of ZnO crystal. In addition, the $T(r)$ of β - $\text{Zn}_2\text{P}_2\text{O}_7$ crystal shown in Supplementary Fig. 5b has two Zn–O atomic distances at 2.03 Å (Zn–O(I)) and at 2.30 Å (Zn–O(II)). The N_{ZnO} calculated up to the first and the second coordination distances are 4 and 2, respectively. Thus, the correlation peak at

2.03 Å of $T(r)$ for β - $\text{Zn}_2\text{P}_2\text{O}_7$ crystal is assigned to tetrahedral coordinated zinc. On the other hand, the Zn–O atomic distance is shorter and the peak area in the ZP glass is smaller than those in ZnO and β - $\text{Zn}_2\text{P}_2\text{O}_7$ crystal. These observations above suggest that the Zn–O coordination in ZP glass is different from that in ZnO and β - $\text{Zn}_2\text{P}_2\text{O}_7$ crystal, although fourfold zinc is dominant in glasses as Walter *et al.* concluded³⁰.

Discussion

Thus, we have succeeded in modelling atomic configurations, which reproduce the X-ray, neutron, EXAFS and NMR data. To understand network formation in the RMC models, the Q^n

distribution was calculated on the basis of the atomic configurations obtained from said models. $Q^0:Q^1:Q^2:Q^3:Q^4$ ratios of 0.8:49.8:49.0:0.4:0 and 33.8:65.8:0.4:0:0, obtained for the 60ZP and the 70ZP, respectively, concurred with the results of NMR shown in Fig. 2b and those reported in previous studies^{29–31,35}. However, although Hoppe *et al.* reported on the structure of ZP glass derived from RMC modelling using X-ray and neutron diffraction data, we are not aware of any structure models that reproduce diffraction, EXAFS and NMR data. Accordingly, it is demonstrated that our model is reliable not at only short-range but also at intermediate range, including the connectivity of polyhedra, because our obtained Q^n distribution was calculated by analysing the –O–P–O– connectivity (not simply estimating on the basis of the coordination numbers reported in ref. 39 (see Methods for details)). The results of Q^n analysis and connectivity of atoms together with coordination numbers are listed in Supplementary Table 4. To understand the connectivity of the network consisting of PO_4 tetrahedra and Zn–O polyhedra in detail, oxygen–cation coordination number distributions were calculated, as shown in Fig. 5. As can be seen in Fig. 5a,b, it is found that OP_2 is more dominant than OZn_2 in 60ZP glass, while OZn_2 is more dominant than OP_2 in 70ZP glass, demonstrating that the role of network formation changes from PO_4 tetrahedra to Zn–O polyhedra between 60ZP and 70ZP, although Fig. 5c suggests that twofold oxygen is taken by an interplay between the PO_4 tetrahedra and Zn–O polyhedra. The change in the role of the network formation from PO_4 tetrahedra to Zn–O polyhedra between 60ZP and 70ZP can explain the behaviour of the thermal expansion coefficient. It is also found that 33% of the oxygen is coordinated by three cations (9% is P2–O–Zn1 and 24% is P1–O–Zn2) in 70ZP glass. Another important feature in oxygen–cation coordination is that the cation coordination numbers are increased in 70ZP glass. To understand such connectivity in 3D atomic configuration, the connectivity of PO_4 and Zn–O polyhedra were analysed. Figure 6 shows the 3D linkage of the phosphate network in terms of the chain length, as calculated from the total number of atoms in each phosphate; Fig. 6a shows the fraction of Q^1 units and Q^2 chains of PO_4 polyhedra in the 60ZP glass and a typical RMC-modelled Q^2 chain. As can be seen in Fig. 6b, the 70ZP glass consists of only isolated PO_4 tetrahedra (Q^0) and P_2O_7 dimers (Q^1). Thus, our RMC models reproduce the modification of the 3D phosphate network as observed by ^{31}P MAS NMR. Similar behaviour is observed in binary silicate and aluminate glass with low glass-forming ability^{40–42}. This observation is significant since low-melting-point phosphate glass is essential to many commercial applications.

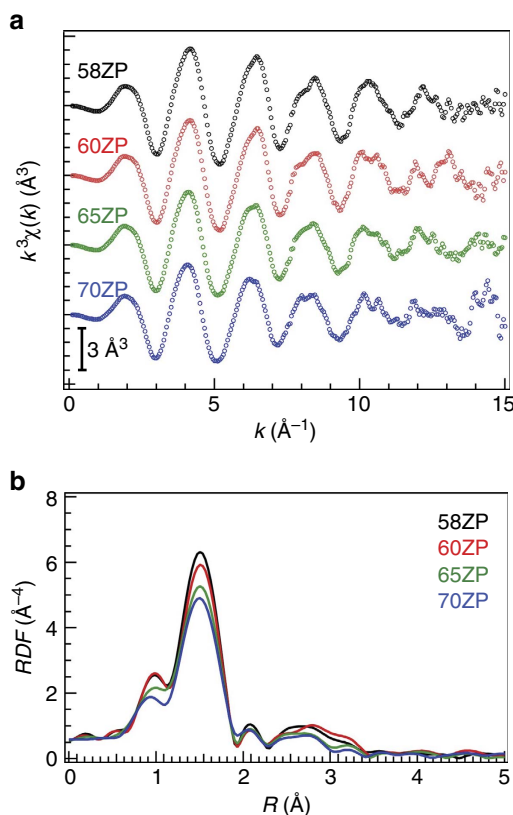


Figure 3 | EXAFS analysis of the ZP glass. (a) EXAFS spectra $k^3\chi(k)$ of the ZnO– P_2O_5 glass and (b) $|FT(R)|$ of the spectra.

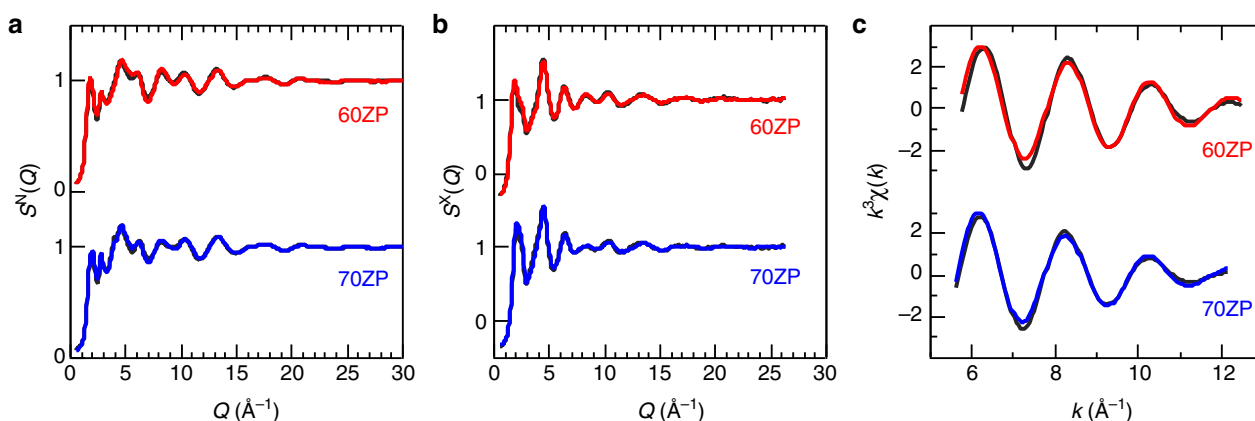


Figure 4 | Comparison between neutron/synchrotron X-ray data and RMC model for the ZP glass. (a) Neutron total structure factor $S^N(Q)$ (b) X-ray total structure factor $S^X(Q)$ and (c) EXAFS $k^3\chi(k)$. The EXAFS $k^3\chi(k)$ were obtained by back Fourier transformation of $|FT(R)|$ of the first correlation peak. Black curve, experimental data; coloured curve, RMC model.

The probabilities of the formation of polyhedral connections between PO_4 tetrahedra and Zn–O polyhedra were calculated (Supplementary Table 5) to elucidate the mechanism of glass formation in binary oxide glass with low amounts of NWF. Corner-sharing between PO_4 – PO_4 , PO_4 –Zn–O polyhedra and Zn–O polyhedra–Zn–O polyhedra occurred predominantly, as stipulated by Zachariasen's rule¹. Both types of ZP glass exhibit the same polyhedral connections, to which their similar T_g and longitudinal modulus can be attributed. Furthermore, the total number of atoms constituting the Zn_xO_y units (Fig. 7) was estimated to determine the origin of the glass network in the glass. As the figure shows, the Zn_xO_y units do not form a network

in 60ZP glass, and the size of the fragment (consisting of up to 41 atoms, as shown in the inset of Fig. 7a) is $< 20 \text{ \AA}$. In contrast, 10% of the Zn_xO_y units in the 70ZP glass form networks consisting of more than 40 atoms, as manifested by their atomic configurations consisting of up to 1,300 atoms, as shown in the inset of Fig. 7b. The unusual network structure units formed by the Zn_xO_y polyhedra can be attributed to the smaller oxygen coordination of the zinc compared to that of the ZnO crystal; the high glass-forming ability of the 70ZP glass stems from this small oxygen coordination. Although the Zn–O coordination number is larger in the RMC model recently reported by Hoppe *et al.*³⁴, they attributed the increased oxygen coordination around the zinc to

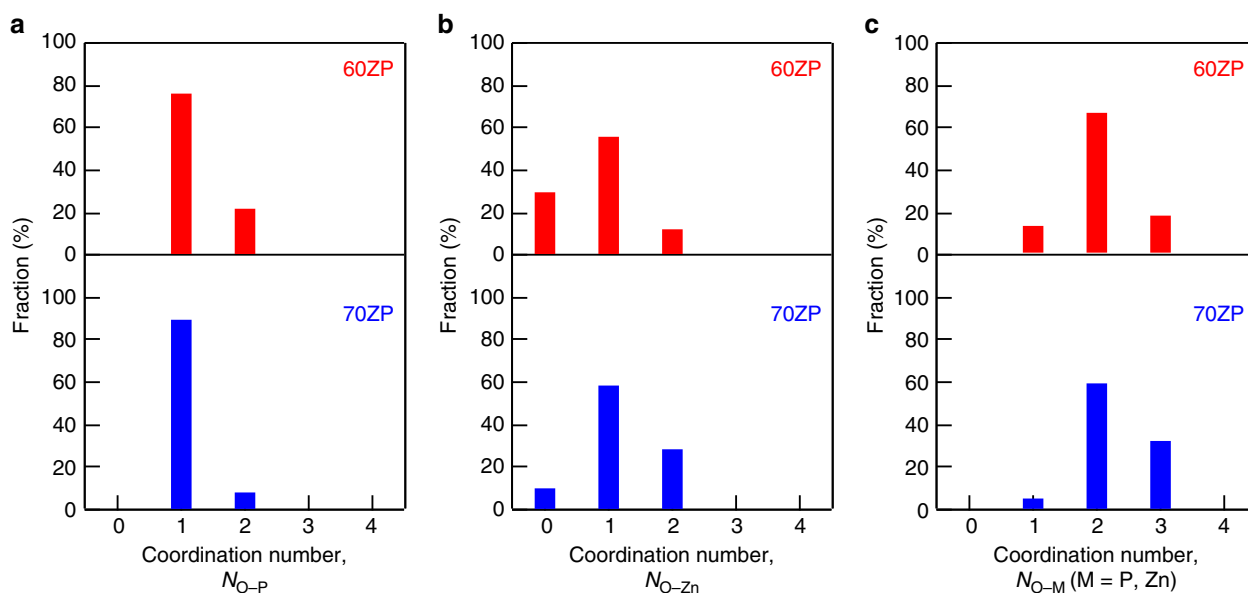


Figure 5 | Oxygen-cation coordination number distribution in the ZP glass. The coordination number distribution of (a) phosphorus, (b) zinc (c) cation (phosphorus and zinc) around oxygen.

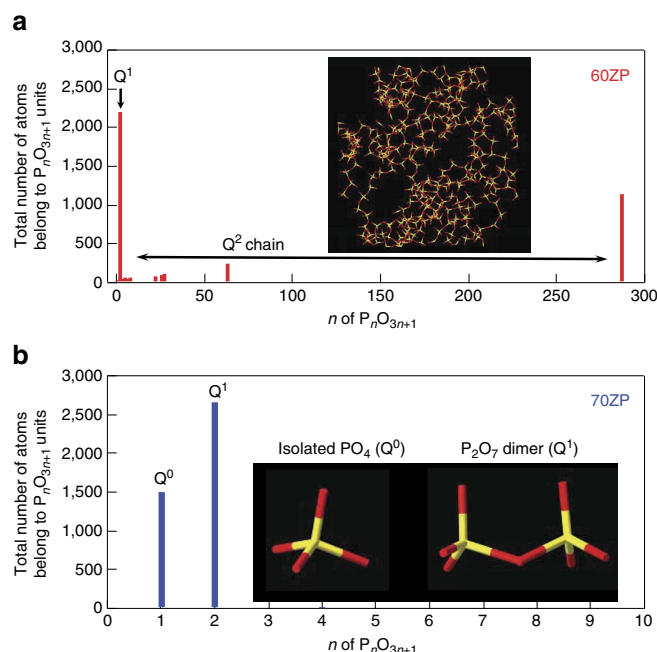


Figure 6 | Connectivity of PO_4 tetrahedra in the ZP glass. The size distribution of PO_4 tetrahedral chains in a 60ZP glass and in b 70ZP glass. P and O atoms are shown in yellow and red colour, respectively.

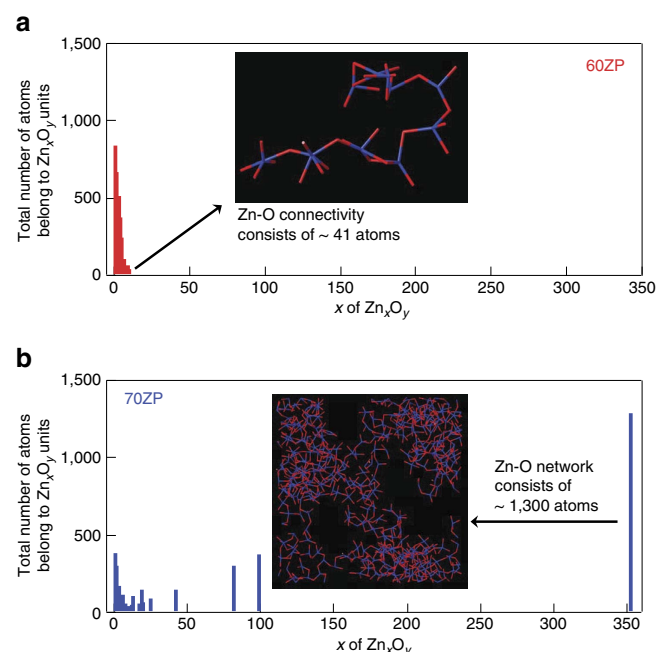


Figure 7 | Connectivity of Zn_xO_y polyhedra in the ZP glass. The size distribution of Zn_xO_y polyhedral chains in a 60ZP glass and in b 70ZP glass. Zn and O atoms are shown in blue and red colour, respectively.

the increased rigidity of the ZP in the 75ZP and 80ZP glass. On the other hand, it is suggested from our RMC model that the small Zn–O coordination is a signature of the NWF, according to Zachariassen's rule¹, in our model for 70ZP glass. This suggestion is supported by the small oxygen–cation coordinations (2.06 in 60ZP and 2.29 in 70ZP) listed in Supplementary Table 4, although the oxygen–cation coordination number is increased in 70ZP glass.

In this study, several types of binary ZnO–P₂O₅ glass are prepared with a wide range of chemical compositions. The present findings regarding the 3D network formation of Zn_xO_y units suggest that interplay between the PO₄ tetrahedra and Zn–O polyhedra is important for tuning the physical properties of the glass. A small Zn–O coordination number might be important for improving the glass-forming ability and to increase the elastic modulus owing to this interplay. On the other hand, the addition of ZnO results in an increased oxygen–cation coordination number, which indicates an increased glass transition temperature, refractive index and packing fraction, and hence longitudinal modulus. Furthermore, we find that the thermal expansion coefficient sensitively reflects the substitution of the phosphate chain network by a network consisting of Zn_xO_y units in zinc-rich glass. In other words, we succeed in revealing, for the first time, the relationship between the atomic structure of glass and its functionality by using structural modelling based on a combination of an advanced quantum beam technique and spectroscopic measurement. Since phosphate glass exhibits a low melting point, then both the phosphate and glass networks consist of counter metal oxides, which give rise to this low-melting-point behaviour. The results obtained in this study, via several structural analysis methods, are significant since they clearly reveal the fundamental properties that determine the functionality of these types of glasses and may be useful in the design of phosphate glasses for practical applications.

Methods

Preparation of binary ZP glass. The different types of binary ZnO–P₂O₅ (xZP) glass, namely, 58ZnO–42P₂O₅ (58ZP), 60ZnO–40P₂O₅ (60ZP), 65ZnO–35P₂O₅ (65ZP) and 70ZnO–30P₂O₅ (70ZP), were prepared by a conventional melt-quenching method using a platinum crucible⁴⁷. Batches consisting of ZnO (99.99%) and (NH₄)₂HPO₄ (99%) were initially calcined at 800 °C for 3 h in an ambient atmosphere. The calcined solid was then melted at 1,100 °C for 30 min in an ambient atmosphere. The glass melt was quenched on a stainless plate maintained at 200 °C and then annealed at the glass transition temperature, *T*_g, for 1 h. The samples were then mechanically polished to produce a mirror surface.

Compositional analysis. Chemical compositions of ZP glasses were determined by using inductively coupled plasma-atomic emission spectrometry analysis using a SPECTRO BLUE (SPECTRO, Germany). The standard solutions (1.5, 10 and 15 p.p.m.) of each element for the calibration curves were prepared by mixing each 1,000 p.p.m. standard solution with 0.1 M HNO₃ solution. The calibration curves at different wavelengths of each element are shown in Supplementary Fig. 1. It was found that the calibration curves show a good linearity for both Zn and P. The concentrations of zinc and phosphorus are calculated by using averaged values of these three emission bands shown in Supplementary Fig. 1. The measured concentration values are summarized in Supplementary Table 1. The ZnO fraction *f*_{ZnO} of the glasses, that is, chemical composition of ZnO–P₂O₅ glasses, can be obtained from both concentration of Zn, *c*_{Zn}, and that of P, *c*_P, by using the following equation:

$$f_{\text{ZnO}} = c_{\text{Zn}} / (c_{\text{Zn}} + (c_{\text{P}}/2)) \times 100 \quad (1)$$

From two samples of each composition, average ZnO fraction can be calculated.

Physicochemical analysis. The *T*_g was determined from thermomechanical analysis (TMA) at a heating rate of 10 °C min^{−1} and under a 1.0 g loading using a TMA 8310 (Rigaku, Japan). The linear thermal expansion coefficient of the samples, measuring around 4 mm × 4 mm × 15 mm, was also evaluated using the same equipment at a temperature range of 200–350 °C. Moreover, the local coordination state of phosphorus was determined by measuring the ³¹P MAS

NMR spectra using a CMX-400 NMR spectrometer (JEOL, Japan). A frequency, spin rate and pulse delay of 161.80 MHz, 10 kHz and 5 s, respectively, were used in the measurements. The chemical shifts were estimated with respect to H₃PO₄ in a D₂O solution (0 p.p.m.) and the conventional notation for phosphorus sites, Q^{*n*}, was used for the analysis. The *n* value denotes the number of bridging oxygens per PO₄ tetrahedron. Furthermore, the densities were measured by applying the Archimedes method using water at room temperature. We measured the refractive index of the samples using a prism coupler with a 473, 633, 1,319 and 1,553 nm light source (Metericon, NJ, USA); the error in the measurement was 10^{−4}.

Elastic modulus measurement. The Brillouin shifts *v*_B of the different types of glass were measured using a high-resolution modification of a Sandercock Fabry–Perot system⁴⁸. A frequency-doubled diode-pumped solid state neodymium:yttrium–aluminium–garnet laser oscillating in a single longitudinal mode at 532 nm (Oxxius SLIM-532 300 mW) was used as the excitation source. In addition to the excitation laser source, a second weak reference laser was also used to act as an independent reference signal that was used for stabilization of the Fabry–Perot. The reference laser was a small diode-pumped solid state neodymium:yttrium–vanadate (Nd:YVO₄) laser module (Photonic Products 300-0088-01, 4 mW) oscillating in single transverse mode (TEM₀₀), which had two to three longitudinal modes separated by 120 GHz. The longitudinal sound velocity *V*_L, shown in Supplementary Table 2, was calculated from *V*_L = *v*_Bλ/2*n*₅₃₂, where *v*_B, λ and *n*₅₃₂ are the Brillouin shift, the wavelength of incident light (= 532 nm) and the refractive index at 532 nm, respectively. The *n*₅₃₂ values were calculated from the Cauchy relationship between the refractive indices at different wavelengths.

EXAFS measurement. The Zn *K*-edge (9.66 keV) EXAFS spectra were measured at the BL01B1 beamline of SPring-8 synchrotron radiation facility (Hyogo, Japan). The measurements were performed using a Si (111) double-crystal monochromator in the transmission mode (Quick Scan method) at room temperature. Pellet samples for the measurements were prepared by mixing the granular sample with boron nitride. The corresponding analyses were performed by using REX2000 software (Rigaku)⁴⁹.

High-energy X-ray diffraction measurement. The high-energy X-ray diffraction experiment was performed at the BL04B2 beamline at the SPring-8 synchrotron radiation facility, using a two-axis diffractometer dedicated to the study of disordered materials⁵⁰. The energy of the incident X-rays was 61.4 keV. The raw data were corrected for polarization, absorption and the background, and the contribution of Compton scattering was subtracted by using standard data analysis software⁵⁰.

RMC modelling. RMC modelling of the 60ZP and the 70ZP glass was performed using RMC++ code⁵¹. The start configurations, which contained 5,000 and 5,250 particles for the 60ZP and the 70ZP, respectively, were created using hard-sphere Monte Carlo simulations with constraints applied to avoid physically unrealistic structures. The *r*-spacing for the calculations of partial-pair correlation functions was set to be 0.05 Å. Two kinds of constraints were used: a closest atom–atom approach and connectivity. The closest atom–atom approach was chosen based on the need to avoid unreasonable spikes in the partial-pair correlation functions. The constraint on the P–O connectivity was that all of the phosphorus atoms were coordinated to four oxygen atoms for atomic distances of up to 1.7 Å. In addition, fixed neighbour constraints⁵² were applied for P–O at 1.55–1.7 Å and P=O at 1.4–1.55 Å to reproduce the Q⁰:Q¹:Q²:Q³ ratio based on the results of the NMR in which the Q⁰:Q¹:Q²:Q³ ratio is 0:50:50:0 for 60ZP and 33.3:66.7:0:0 for 70ZP. After the hard-sphere Monte Carlo simulations, RMC simulations containing X-ray S(Q), neutron S(Q) and *k*²χ(*k*) EXAFS data, measured at the Zn *K*-edge, were performed. The EXAFS back scattering tables were obtained from FEFF calculations⁵³.

Data availability. The authors declare that all relevant data supporting the findings of this study are available from the corresponding authors on request.

References

- Zachariassen, W. H. The atomic arrangement in glass. *J. Am. Chem. Soc.* **54**, 3841–3851 (1932).
- Warren, B. E. & Biscoe, J. The structure of silica glass by X-ray diffraction studies. *J. Am. Ceram. Soc.* **21**, 49–54 (1938).
- Du, J. & Cormack, A. N. The medium range structure of sodium silicate glasses: a molecular dynamics simulation. *J. Non-Cryst. Solids* **349**, 66–79 (2004).
- Du, J. & Corrales, L. R. First sharp diffraction peak in silicate glasses: structure and scattering length dependence. *Phys. Rev. B* **72**, 092201 (2005).

5. Du, J. & Corrales, L. R. Compositional dependence of the first sharp diffraction peaks in alkali silicate glasses: a molecular dynamics study. *J. Non-Cryst. Solids* **352**, 3255–3269 (2006).
6. Pedone, A., Malavasi, G., Cormack, A. N., Segre, U. & Menziani, M. C. Insight into elastic properties of binary alkali silicate glasses; prediction and interpretation through atomistic simulation techniques. *Chem. Mater.* **19**, 3144–3154 (2007).
7. Brow, R. K. Review: the structure of simple phosphate glasses. *J. Non-Cryst. Solids* **263–264**, 1–28 (2000).
8. Martin, S. W. Review of the structure of phosphate glasses. *Euro. J. Solid State Inorg. Chem.* **28**, 163–205 (1991).
9. Hoppe, U. A structural model for phosphate glasses. *J. Non-Cryst. Solids* **195**, 138–147 (1996).
10. Sayer, M. & Mansingh, A. Transport properties of semiconducting phosphate glasses. *Phys. Rev. B* **6**, 4629–4643 (1972).
11. Masai, H. *et al.* ^{31}P NMR and IR study of highly water-stable $\text{SrO-BaO-Nb}_2\text{O}_5\text{-P}_2\text{O}_5$ glass and glass-ceramics. *Chem. Lett.* **42**, 1305–1307 (2013).
12. Takamatsu, Y. *et al.* The state of $\text{P}=\text{O}_{\text{nb}}$ non-bridging oxygen and proton incorporation in binary $\text{MO} \cdot \text{P}_2\text{O}_5$ ($\text{M} = \text{Ca, Mg}$) phosphate glasses. *Solid State Ionics* **245–246**, 19–23 (2013).
13. Bunker, B. C., Arnold, G. W. & Wilder, J. A. Phosphate glass dissolution in aqueous solutions. *J. Non-Cryst. Solids* **64**, 291–316 (1984).
14. Kokubo, T. & Takadama, H. How useful is SBF in predicting *in vivo* bone bioactivity? *Biomaterials* **27**, 2907–2915 (2006).
15. Paulose, P. I., Jose, G., Thomas, V., Unnikrishnan, N. V. & Warriar, M. K. R. Sensitized fluorescence of $\text{Ce}^{3+}/\text{Mn}^{2+}$ system in phosphate glass. *J. Phys. Chem. Solids* **64**, 841–846 (2003).
16. Campbell, J. H. & Suratwala, T. I. Nd-doped phosphate glasses for high-energy/high-peak-power lasers. *J. Non-Cryst. Solids* **263**, 318–341 (2000).
17. Yan, Y. C., Faber, A. J., de Waal, H., Kik, P. G. & Polman, A. Erbium-doped phosphate glass waveguide on silicon with 4.1 dB/cm gain at 1.535 μm . *Appl. Phys. Lett.* **71**, 2922–2924 (1997).
18. Inaba, S., Hosono, H. & Ito, S. Entropic shrinkage of an oxide glass. *Nat. Mater.* **14**, 312–317 (2015).
19. Brow, R. K. & Tallant, D. R. Structural design of sealing glasses. *J. Non-Cryst. Solids* **222**, 396–406 (1997).
20. Morena, R. Phosphate glasses as alternatives to Pb-based sealing frits. *J. Non-Cryst. Solids* **263–264**, 382–387 (2000).
21. Joshi, B. C. Enhanced Eu^{3+} emission by nonradiative energy-transfer from Tb^{3+} in zinc phosphate glass. *J. Non-Cryst. Solids* **180**, 217–220 (1995).
22. Caldino, U., Hernandez-Pozos, J. L., Flores, C., Speghini, A. & Bettinelli, M. Photoluminescence of Ce^{3+} and Mn^{2+} in zinc metaphosphate glasses. *J. Phys.: Condens. Matter* **17**, 7297–7305 (2005).
23. Masai, H., Takahashi, Y., Fujiwara, T., Matsumoto, S. & Yoko, T. High photoluminescent property of low-melting Sn-doped phosphate glass. *Appl. Phys. Express* **3**, 082102 (2010).
24. Masai, H. *et al.* White light emission of Mn-doped $\text{SnO-ZnO-P}_2\text{O}_5$ glass containing no rare earth cation. *Opt. Lett.* **36**, 2868–2870 (2011).
25. Masai, H. *et al.* Correlation between emission property and concentration of Sn^{2+} centre in the $\text{SnO-ZnO-P}_2\text{O}_5$ glass. *Opt. Express* **20**, 27319–27326 (2012).
26. Özgür, Ü. A comprehensive review of ZnO materials and devices. *J. Appl. Phys.* **98**, 041301 (2005).
27. Onyiriuka, E. C. Zinc phosphate glass surfaces studied by XPS. *J. Non-Cryst. Solids* **163**, 268–273 (1993).
28. Brow, R. K. An XPS study of oxygen bonding in zinc phosphate and zinc borophosphate glasses. *J. Non-Cryst. Solids* **194**, 267–273 (1996).
29. Brow, R. K., Tallant, D. R., Myers, S. T. & Phifer, C. C. The short-range structure of zinc polyphosphate glass. *J. Non-Cryst. Solids* **191**, 45–55 (1995).
30. Walter, G., Hoppe, U., Vogel, J., Carl, G. & Hartmann, P. The structure of zinc polyphosphate glass studied by diffraction methods and ^{31}P NMR. *J. Non-Cryst. Solids* **333**, 252–262 (2004).
31. Wiench, J. W., Pruski, M., Tischendorf, B., Otaigbe, J. U. & Sales, B. C. Structural studies of zinc polyphosphate glasses by nuclear magnetic resonance. *J. Non-Cryst. Solids* **263–264**, 101–110 (2000).
32. Hoppe, U. *et al.* Combined neutron and X-ray scattering study of phosphate glasses. *J. Non-Cryst. Solids* **293–295**, 158–168 (2001).
33. Walter, G., Hoppe, U., Baade, T., Kranold, R. & Stachel, D. Intermediate range order in $\text{MeO-P}_2\text{O}_5$ glasses. *J. Non-Cryst. Solids* **217**, 299–307 (1997).
34. Hoppe, U., Dimitriev, Y. & Jónvári, P. Structure of zinc phosphate glasses of 75 and 80 mole% ZnO content studied by X-ray diffraction and reverse Monte Carlo simulations. *Z. Naturforsch.* **60**, 517–526 (2005).
35. Tischendorf, B., Otaigbe, J. U., Wiench, J. W., Pruski, M. & Sales, B. C. A study of short and intermediate range order in zinc phosphate glasses. *J. Non-Cryst. Solids* **282**, 147–158 (2001).
36. Saout, G. L. *et al.* A multispectroscopic study of $\text{PbO}_x\text{ZnO}_{0.6-x}(\text{P}_2\text{O}_5)_{0.4}$ glasses. *J. Non-Cryst. Solids* **293–295**, 657–662 (2001).
37. Tischendorf, B., Alam, T. M., Cygan, R. T. & Otaigbe, J. U. The structure and properties of binary zinc phosphate glasses studied by molecular dynamics simulations. *J. Non-Cryst. Solids* **316**, 261–272 (2003).
38. Suzuya, K., Itoh, K., Kajinami, A. & Loong, C.-K. The structure of binary zinc phosphate glasses. *J. Non-Cryst. Solids* **345**, 80–87 (2004).
39. Hoppe, U., Walter, G., Carl, G., Neufeind, J. & Hannon, A. C. Structure of zinc phosphate glasses probed by neutron and X-ray diffraction of high resolving power and by reverse Monte Carlo simulations. *J. Non-Cryst. Solids* **351**, 1020–1031 (2005).
40. Kohara, S. *et al.* Glass formation at the limit of insufficient network formers. *Science* **303**, 1649–1652 (2004).
41. Kohara, S. *et al.* Relationship between topological order and glass forming ability in densely packed enstatite and forsterite composition glasses. *Proc. Natl Acad. Sci. USA* **108**, 14780–14785 (2011).
42. Akola, J. *et al.* Network topology for the formation of solvated electrons in binary $\text{CaO-Al}_2\text{O}_3$ composition glasses. *Proc. Natl Acad. Sci. USA* **110**, 10129–10134 (2013).
43. Kohara, S. *et al.* Atomic and electronic structures of an extremely fragile liquid. *Nat. Commun.* **5**, 5892 (2014).
44. Tomozawa, M., Takata, M., Acocella, J., Watson, E. B. & Takamori, T. Thermal properties of $\text{Na}_2\text{O-3SiO}_2$ glasses with high water content. *J. Non-Cryst. Solids* **56**, 343–348 (1983).
45. Shelby, J. E. Thermal expansion of alkali borate glasses. *J. Am. Ceram. Soc.* **66**, 225–227 (1983).
46. Kirkpatrick, R. J. & Brow, R. K. Nuclear magnetic resonance investigation of the structures of phosphate and phosphate-containing glasses: a review. *Solid State Nucl. Mag.* **5**, 9–21 (1995).
47. Masai, H. *et al.* Fabrication of Sn-doped zinc phosphate glass using a platinum crucible. *J. Non-Cryst. Solids* **358**, 265–269 (2012).
48. Koreeda, A. & Saikan, S. Note: higher resolution Brillouin spectroscopy by offset stabilization of a tandem Fabry-Pérot interferometer. *Rev. Sci. Instrum.* **82**, 126103 (2011).
49. Taguchi, T., Ozawa, T. & Yashiro, H. REX2000: yet another XAFS analysis package. *Phys. Scripta* **T115**, 205–206 (2005).
50. Kohara, S. *et al.* Structural studies of disordered materials using high-energy x-ray diffraction from ambient to extreme conditions. *J. Phys. Condens. Matter* **19**, 506101 (2007).
51. Gereben, O., Jónvári, P., Temleitner, L. & Pusztai, L. A new version of the RMC++ , reverse Monte Carlo programme, aimed at investigating the structure of covalent glasses. *J. Optoelectron. Adv. Mater.* **9**, 3021–3027 (2007).
52. Evrard, G. & Pusztai, L. Reverse Monte Carlo modelling of the structure of disordered materials with RMC++ : a new implementation of the algorithm in C++ . *J. Phys. Condens. Matter* **17**, S1–S13 (2005).
53. Ankudinov, A. L., Ravel, B., Rehr, J. J. & Conradson, S. D. Real-space multiple-scattering calculation and interpretation of X-ray-absorption near-edge structure. *Phys. Rev. B* **58**, 7565–7576 (1998).

Acknowledgements

This work was partially supported by the JSPS KAKENHI Grant-in-Aid for Young Scientists (A) Number 26709048, the Izumi Science and Technology Foundation and the Collaborative Research Program of I.C.R., Kyoto University (grant Nos. 2015-69 and 2016-47). We thank Prof Y. Sohrin, Dr T. Minami and Mr M. Tsujisaka (I.C.R., Kyoto University) for supporting the inductively coupled plasma-atomic emission spectrometry measurement. The synchrotron radiation experiments were performed at the BL01B1 and the BL04B2 of SPring-8 with the approval of the Japan Synchrotron Radiation Research Institute (JASRI; Proposal Nos. 2013A1412, 2014A1134, 2015A1311, 2016A0130 and 2016A0134). We thank Dr T. Ina for supporting the EXAFS measurements at the BL01B1. This work was also supported by JST-PRESTO 'Advanced Materials Informatics through Comprehensive Integration among Theoretical, Experimental, Computational and Data-Centric Sciences' (JPMJPR15N4) and the 'Materials Research by Information Integration' Initiative (MI2I) project of the Support Program for Starting Up Innovation Hub from JST. We gratefully acknowledge Dr K. Suzuya for providing us with the neutron diffraction data for $\text{ZnO-P}_2\text{O}_5$.

Author contributions

H.M. and S.K. formulated the research project; H.M. and S.O. performed the materials preparation and EXAFS analysis; H.M. and A.K. measured the elastic modulus using Brillouin scattering; H.M. performed the thermal expansion, refractive index and inductively coupled plasma-atomic emission spectrometry measurements; T.O. measured ^{31}P MAS NMR spectra and analysed the resulting data; S.K. performed X-ray diffraction measurements and analysed the resulting data; Y.O. and S.K. performed RMC modelling; Y.O., H.M. and S.K. wrote the paper.

Additional information

Supplementary Information accompanies this paper at <http://www.nature.com/naturecommunications>

Competing interests: The authors declare no competing financial interests.

Reprints and permission information is available online at <http://npg.nature.com/reprintsandpermissions/>

How to cite this article: Onodera, Y. *et al.* Formation of metallic cation-oxygen network for anomalous thermal expansion coefficients in binary phosphate glass. *Nat. Commun.* **8**, 15449 doi: 10.1038/ncomms15449 (2017).

Publisher's note: Springer Nature remains neutral with regard to jurisdictional claims in published maps and institutional affiliations.



This work is licensed under a Creative Commons Attribution 4.0 International License. The images or other third party material in this article are included in the article's Creative Commons license, unless indicated otherwise in the credit line; if the material is not included under the Creative Commons license, users will need to obtain permission from the license holder to reproduce the material. To view a copy of this license, visit <http://creativecommons.org/licenses/by/4.0/>

© The Author(s) 2017